Multiband Electrostatic Waves below and above the Electron Cyclotron Frequency in the Near-Sun Solar Wind

Chen Shi[1,2], Jinsong Zhao[1,2], David M. Malaspina[3,4], Stuart D. Bale[5,6], Xiangcheng Dong[7], Tieyan Wang[8], and Dejin Wu[1]

[1] Purple Mountain Observatory, Chinese Academy of Sciences, Nanjing 210023, People's Republic of China; js_zhao@pmo.ac.cn
[2] School of Astronomy and Space Science, University of Science and Technology of China, Hefei 230026, People's Republic of China
[3] Astrophysical and Planetary Sciences Department, University of Colorado, Boulder, CO, USA
[4] Laboratory for Atmospheric and Space Physics, University of Colorado, Boulder, CO, USA
[5] Physics Department, University of California, Berkeley, CA 94720-7300, USA
[6] Space Sciences Laboratory, University of California, Berkeley, CA 94720-7450, USA
[7] RAL Space, STFC, Oxfordshire OX11 0QX, UK
[8] School of Earth Science, Yunnan University, Kunming 650091, People's Republic of China

Abstract

Using the Parker Solar Probe measurements, this Letter reports two new types of multiband electrostatic waves in and near the heliospheric current sheet. They are classified into the $f < f_{ce}$ and $f > f_{ce}$ multiband electrostatic waves, in which most (or all) of the bands in the former type are lower than f_{ce}, and all of the bands in the latter type are higher than f_{ce}, where f and f_{ce} denotes the wave frequency and the electron cyclotron frequency, respectively. This Letter also exhibits observational evidence of the existence of nonlinear wave–wave interactions of both types of electrostatic waves. In particular, the $f > f_{ce}$ multiband electrostatic waves are found to be modulated in the presence of low-frequency oblique ion-scale waves. According to the observed frequency distribution, this Letter proposes that the mode nature of the $f < f_{ce}$ multiband electrostatic waves could be the oblique ion acoustic wave or the lower-hybrid wave, and the $f > f_{ce}$ multiband electrostatic waves are the electron Bernstein mode wave. These findings provide a challenge to understand the complex electron and ion dynamical processes in and near the heliospheric current sheet.

Unified Astronomy Thesaurus concepts: Space plasmas (1544); Plasma physics (2089); Solar wind (1534)

1. Introduction

One mystery in the solar atmosphere and the near-Sun solar wind is how the energetic particle population and the associated high-frequency waves interact with each other and evolve. When these energetic particles contain free energy behaving (possibly, but not the only possibility) as the beam, ring, ring beam, or loss cone in the particle velocity distribution function, they can radiate different kinds of high-frequency plasma waves (e.g., whistler waves, ion acoustic waves, electron acoustic waves, electron Bernstein waves, and high-frequency electromagnetic waves) under different plasma parameters (e.g., Ashour-Abdalla & Kennel 1978; Umeda et al. 2007; Chen et al. 2020; Shi et al. 2020; Wu et al. 2020; Zhou et al. 2020; Sun et al. 2021). Before the launch of the Parker Solar Probe (PSP; Fox et al. 2016), only remote radio observations could enable indirect conjectures regarding the dynamical process between high-frequency waves and high-energy electrons in the solar atmosphere and its neighborhood (e.g., Bastian et al. 1998). Nowadays, in situ measurements by PSP provide a unique opportunity to directly investigate both high-frequency waves and high-energy particles in the inner heliosphere. This Letter focuses on high-frequency waves between the lower-hybrid frequency f_{LH} and the electron plasma frequency f_{pe} detected by PSP.

From PSP observations, Malaspina et al. (2020) first reported the existence of multiband high-frequency electrostatic waves in the near-Sun solar wind below 50 solar radii, in which the wave power densities are peaked at the frequency $f \sim 0.7 f_{ce}$ and $f \sim f_{ce}$ and their harmonics (also see Ma et al. 2021), where f_{ce} is the electron cyclotron frequency. Malaspina et al. (2020) also found that these waves preferentially are located in the region where the magnetic field is quiet and nearly following the Parker spiral lines. The detected waves at $f \sim f_{ce}$ are proposed to be the electron Bernstein wave; however, the nature of the waves at $f \sim 0.7 f_{ce}$ is unknown (Malaspina et al. 2021). Malaspina et al. (2021) further found two new types (Type B and Type C) of narrowband electrostatic waves near f_{ce} in a steady magnetic field environment; however, their mode nature is still unknown. Moreover, ion acoustic waves extending to the ion plasma frequency f_{pi} were observed in the near-Sun solar wind (Mozer et al. 2020, 2021a). Mozer et al. (2021b) recently found a new continuous narrowband electrostatic wave below f_{pi}, which is interpreted as the ion acoustic mode wave.

Based on PSP measurements, this Letter will report two new types of multiband electrostatic waves observed in and near the heliospheric current sheet. Their frequency distributions are obviously different from the electrostatic waves found by Malaspina et al. (2020, 2021) and Mozer et al. (2021b). According to their frequency distribution features, they are classified into the $f < f_{ce}$ and $f > f_{ce}$ multiband electrostatic waves. For the $f < f_{ce}$ type waves, most (sometimes all) of the frequency bands are below f_{ce}, and for the $f > f_{ce}$ type waves all of the frequency bands are above f_{ce}. Moreover, this Letter will provide direct observational evidence for nonlinear wave−wave interactions relating to both the $f < f_{ce}$ and $f > f_{ce}$ multiband electrostatic waves.

2. Data and Event Overview

We analyze the data from 20:30:00 UT on 2020 September 24 to 00:00:00 UT on 2020 September 26 measured by PSP, which is in Solar Encounter 6 and at ∼28 solar radii (∼0.13 au). The plasma parameters including the solar wind velocity, the proton number density, the proton temperature, and the electron pitch angle distribution are measured by the SWEAP instrument suite (Kasper et al. 2016). The magnetic and electric field data come from the FIELDS (Bale et al. 2016). The magnetic field from the FGM has a resolution of ∼292 Hz. The electric field spectra we use include AC-coupled survey spectra with a ∼0.9 s cadence and DC-coupled survey spectra with a ∼28 s cadence. The electric field waveform burst data are sampled at 35,000 per second in E6 (Malaspina et al. 2016). In addition, we use the FIELDS RFS electric field spectrum to estimate the electron number density by using the QTN method (Moncuquet et al. 2020).

Figure 1 presents an overview of our high-frequency wave event. Spectrograms of the AC and DC differential voltage V_{12} power spectra are presented in Figures 1(a) and (b), respectively, where the white solid line denotes f_{ce}. We see that multiband electrostatic waves near f_{ce} appear from ∼22:00:00 UT on 2020 September 24 to ∼05:30:00 UT on 2020 September 25 (labeled by Regime I in Figures 1(a)). The frequency distribution of these observed waves is similar to that of the waves found by Malaspina et al. (2020, 2021), i.e., in the wave power centering at ∼0.7f_{ce} and ∼f_{ce}, as well as the harmonics. We also find two more new types of multiband electrostatic waves during ∼08:30:00−19:30:00 UT on 2020 September 25 (labeled by Regime II in Figures 1(a)), in which the strongest wave power is either lower than f_{ce} or higher than f_{ce}.

Different from electrostatic waves near f_{ce} that mainly occupy a steadily radial magnetic field environment (Regime I; $|B_R| \gtrsim 2|B_{T,N}|$), the new types of electrostatic waves arise in a relatively disturbed magnetic field environment (Regime II), as shown by the magnetic field distribution in Figure 1(c). We also filter the three magnetic field components in the low-frequency range of 0.001–1 Hz to quantify the disturbed magnetic field in Regime I and Regime II, and we find that the averaged peak of the disturbed magnetic field is about 0.02 (0.1) times the background magnetic field in Regime I (II). Figure 1(c) further shows that the direction of the magnetic field is radially outward (inward) before (after) the PSP crosses Regime II, and the magnetic field direction roughly changes five times in Regime II. Moreover, from the distributions of the solar wind speed (Figure 1(d)), the proton and electron density (Figure 1(e)), and the proton temperature (Figure 1(f)), we see that the averaged solar wind speed and the proton temperature in Regime II are nearly the same as those in Regime I; however, the proton density in Regime II is nearly 4–8 times larger than that in Regime I. Furthermore, to identify the magnetic configuration, Figure 1(g) presents the pitch angle θ distribution of electrons with an energy of 315 eV. The $\theta \sim 0°$ and 180° outside Regime II indicate the existence of the steady open magnetic field, because the strahl electrons stream outward from the Sun in the open magnetic field. The pitch angle of these strahl electrons is broader in Regime II. According to the observed distributions of the magnetic field and the pitch angle distribution of the strahl electrons, we conclude that the two new types of electrostatic waves in Figure 1 occur in and nearby the heliospheric current sheet.

In order to illustrate the difference between these new types of multiband electrostatic waves and the multiband waves found by Malaspina et al. (2020), we will exhibit their electric field spectra in four typical events (occurring at ∼10:24:07, 15:08:56, 15:37:39, and 18:24:13 UT on 2020 September 25) labeled by the dashed–dotted lines in Figure 1.

3. The $f < f_{ce}$ and $f > f_{ce}$ Multiband Electrostatic Waves

We plot all spectral power densities (PSDs) of the burst mode data from the electric field measurement in Regime II. Of all 49 burst mode events on 2020 September 25, 29 events contain only the $f < f_{ce}$ multiband electrostatic waves, 5 events contain the $f > f_{ce}$ multiband electrostatic waves, and 3 events contain both types of waves. We choose four typical events to illustrate the main features of the observed waves (see Figure 1): Event #1 and Event #2 for the $f < f_{ce}$ multiband electrostatic waves, Event #4 for the $f > f_{ce}$ multiband electrostatic waves, and Event #3 for the mix of two types of waves.

First, we analyze the $f < f_{ce}$ type multiband electrostatic waves in Events #1 and #2, in which the strongest wave power occurs below the f_{ce}.

Figures 2(a1)–(f1) present the PSDs of the electric fields E_x and E_y and summarize the information of the peak, bandwidth, and amplitude in each frequency band in Event #1. The solid and dotted curves in Figures 2(a1) and (d1) denote, respectively, $f_{ce} \simeq 801$ Hz and $f_{LH} \simeq 19$ Hz under the averaged magnetic field strength $B_0 \simeq 28.6$ nT. There exist six frequency bands in both the E_x and E_y PSDs. The first frequency band where the frequency is lowest contains the strongest wave power peaking at $f_1 \simeq 200$ Hz $\simeq 0.25 f_{ce}$ (or $\simeq 11 f_{LH}$). The other frequency bands center at the harmonics of f_1, and the highest frequency band is higher than the f_{ce}. The wave amplitudes $\delta E_x(f_n)$ and $\delta E_y(f_n)$, shown in Figures 2(c1) and (f1), are obtained by filtering the electric field data in the frequency range $[f_n - \Delta f_n/2, f_n + \Delta f_n/2]$, where $n = 1, ..., 6$ denotes the number of the frequency band. We can see that both of the wave amplitudes decrease with increasing n, which implies the possibility that the harmonic waves ($n > 1$) are excited by the nonlinear interaction of the fundamental band wave ($n = 1$).

Figures 2(a2)−(f2) present the PSDs of the two electric field components and their key parameters in Event #2. The lowest frequency $f_1 \simeq 260$ Hz $\simeq 0.08 f_{ce}$ (or $\simeq 3 f_{LH}$). Different from Event #1, the highest frequency band does not exceed f_{ce} in Event #2. Also, the wave amplitude $\delta E(f_2) = [\delta E_x^2(f_2) + \delta E_y^2(f_2)]^{1/2} \simeq 2.72$ mV m^{-1} in the second frequency band is larger than that in the first frequency band, i.e., $\delta E(f_1) = [\delta E_x^2(f_1) + \delta E_y^2(f_1)]^{1/2} \simeq 2.42$ mV m^{-1}. Consequently, these two band waves could be emitted independently. According to the wave amplitudes in Event #2, the bands centered at f_{2j+1} can be classified as one subgroup, and the bands at f_{2j+2} correspond to another subgroup, where $j = 1, ..., 5$. The amplitude of the f_{2j+2} band wave is normally larger than that of the f_{2j+1} band wave at the same j. Moreover, f_{2j+1} approximates the sum of f_{2j} and f_1. Therefore, we conclude that one source of the f_{2j+1} band wave could be the nonlinear interaction between the f_{2j} and f_1 band waves. We note that the nonlinear interactions among the second band waves can generate the f_{2j} band waves.

Here, we summarize the basic features of the $f < f_{ce}$ multiband electrostatic waves: (1) the strongest wave power arises at a frequency much smaller than f_{ce}; (2) the waves can extend to the frequency larger than f_{ce}; and (3) the nonlinear wave−wave interactions are evident in the presence of the two band waves with the finite amplitude.
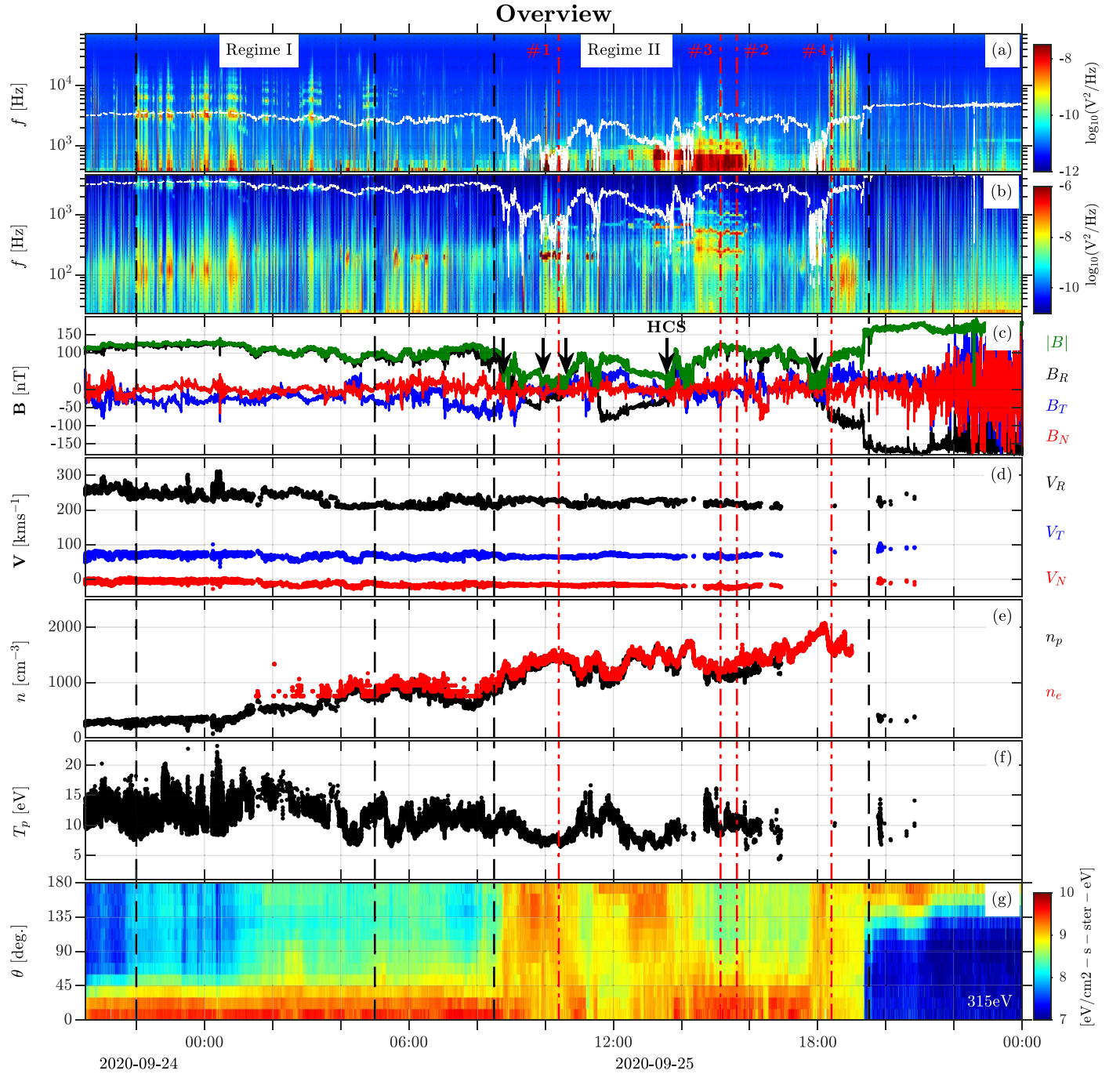
Figure 1. Event overview. (a) Spectrogram of the AC-coupled differential voltage signals of V_{12}. (b) Spectrogram of the DC-coupled differential voltage signals of V_{12}. (c) The magnetic field strength $|B|$ and magnetic field components in RTN coordinates. (d) The solar wind speed in RTN coordinates. (e) The proton number density n_p from SPC and the electron number density estimated by using the QTN method. (f) The proton thermal temperature. (g) The electron pitch angle distribution of electrons with energy $E_e = 315$ eV. The solid white curves in panels (a) and (b) denote the electron cyclotron frequency f_{ce}. The regime permeating multiband electrostatic waves near f_{ce} is labeled Regime I, where the time interval is from 20:00:00 UT on 2020 September 24 to 05:30:00 UT on 2020 September 25. The regime containing the two new types of electrostatic waves is labeled Regime II, where the time interval is from 08:30:00 UT to 19:30:00 UT on 2020 September 25. The times of the four typical events #1−#4 analyzed in later figures are labeled by the red dashed lines. The arrows in panel (c) indicate the position of the heliospheric current sheet (HCS).

Now, we proceed with the analysis of the $f > f_{ce}$ multiband electrostatic waves in Events #3 and #4. These waves have distinct frequency distributions, as shown in Figures 3 and 4.

Figure 3 shows the $f > f_{ce}$ multiband electrostatic waves in Event #3. These waves have four frequency bands, in which the powers center at ~1.7f_{ce}, 2.5f_{ce}, 3.3f_{ce}, and 4.2f_{ce}. The $f < f_{ce}$

multiband electrostatic waves also arise in Event #3, in which the observed features are similar to those in Event #2. Moreover, Event #3 contains the Type B narrowband electrostatic wave found by Malaspina et al. (2021). A new finding of the Type B narrowband electrostatic wave is the coexistence of fundamental and second harmonic waves (see Figure 3(a)).
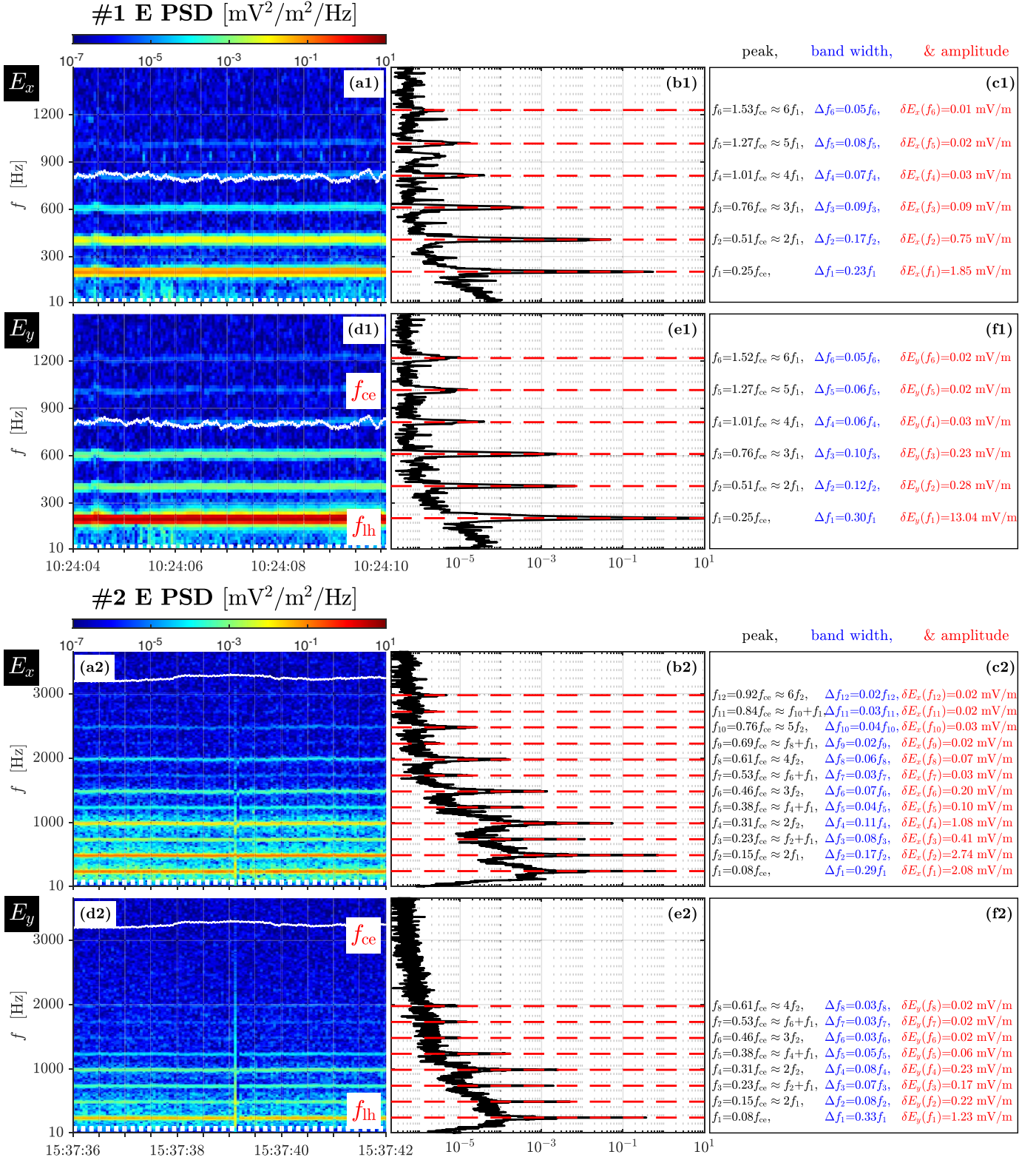
Figure 2. The PSDs of the electric field components E_x and E_y and the wave parameters in Events #1 and #2. Panels (a1)−(c1): spectrogram of the E_x PSD, the averaged E_x PSD, and wave parameters including the peak, bandwidth, and amplitude in each E_x frequency band in Event #1. Panels (d1)−(g1): spectrogram of the E_y PSD, the averaged E_y PSD, and wave parameters including the peak, bandwidth, and amplitude in each E_y frequency band in Event #1. Panels (a2)−(g2) for Event #2: the description is the same as for panels (a1)−(g1). The solid and dotted white lines denote the electron cyclotron frequency f_{ce} and the lower-hybrid frequency f_{LH}, respectively.

Figure 4 shows the $f > f_{ce}$ multiband electrostatic waves in Event #4. The four bands are nearly centered at $3.9f_{ce}$, $4.9f_{ce}$, $5.6f_{ce}$, and $6.8f_{ce}$. Actually, the number of the frequency bands is more than four (the band higher than 17,500 Hz cannot be measured due to the burst data sample rate used on 2020 September 25). Moreover, these four bands are higher than the ion plasma frequency f_{pi}.
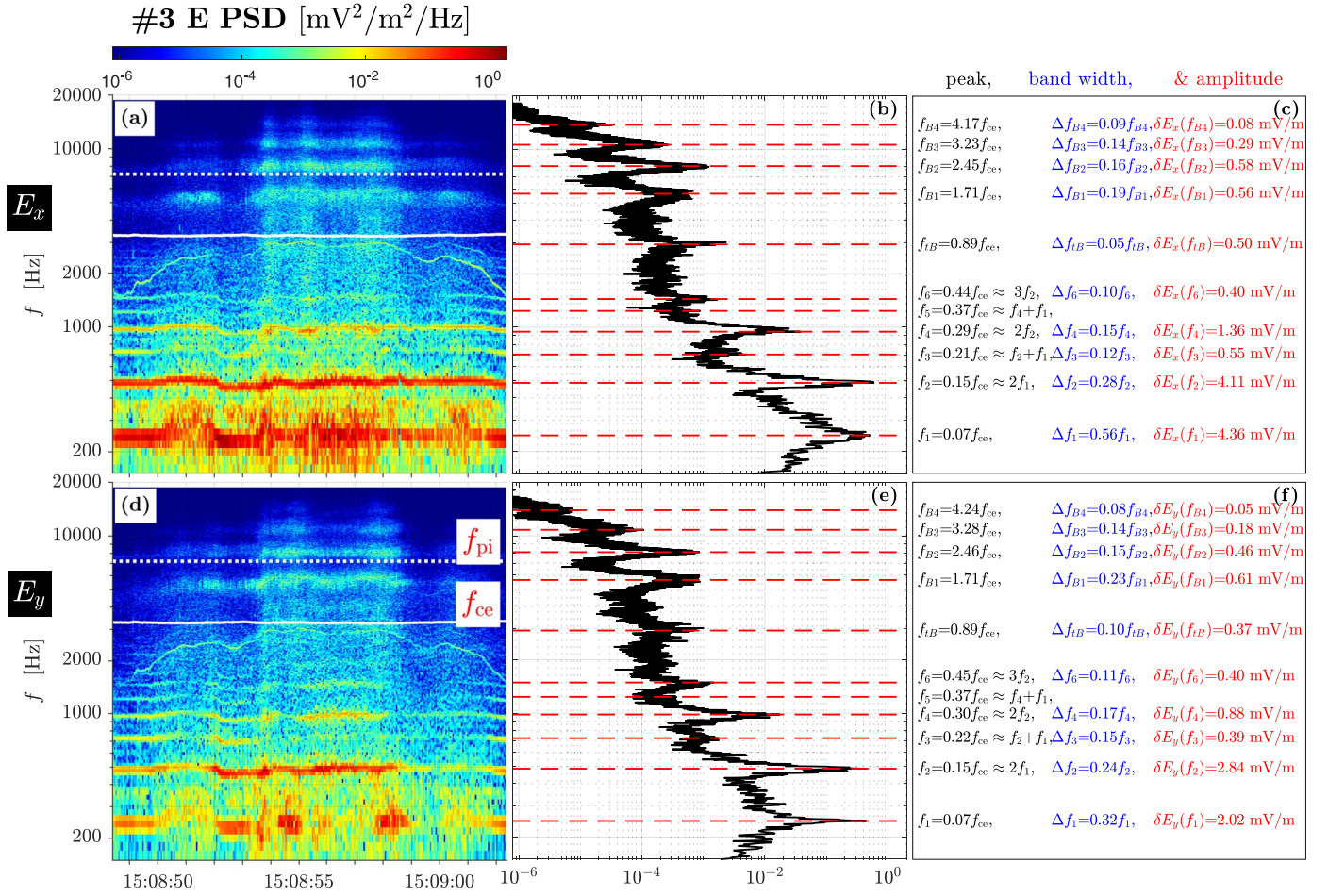
4

Figure 3. The PSDs of the electric field components E_x and E_y and the wave parameters in Event #3. The description of panels (a)−(g) is the same as that in Figure 2. The solid and dashed white curves represent the electron cyclotron frequency f_{ce} and the ion plasma frequency f_{pi}, respectively.

Another important finding in Figure 4 is the modulation of the $f > f_{\mathrm{ce}}$ multiband electrostatic waves by low-frequency waves. Figures 4(a) and (d) exhibit the periodical change of the wave power at a timescale of $\sim 1/3$ s. This timescale is coincident with the period of oblique ion-scale waves appearing in Event #4 (not shown). Figures 4(g)–(j) present the wavelet cross-coherence spectra between the strength of the $f > f_{\mathrm{ce}}$ multiband electrostatic waves and the magnetic field perturbations of oblique ion-scale waves to exhibit their correlation. Here, we use the following procedures to obtain the strength of the $f > f_{\mathrm{ce}}$ multiband electrostatic waves: (1) both δE_x and δE_y in burst data are filtered in the range [f_{pi}, 17,500 Hz]; and (2) the filtered field strength, $|\delta E_x(f > f_{\mathrm{pi}})|$ and $|\delta E_y(f > f_{\mathrm{pi}})|$, are resampled at the FGM resolution. For the magnetic field perturbations δB_x and δB_y of low-frequency waves, they are filtered in the range 1–10 Hz. Figures 4(g)–(j) illustrate that the high correlation coefficients ($\gtrsim 0.75$) arise at $f \sim 3$ Hz as the $f > f_{\mathrm{ce}}$ multiband electrostatic waves have a finite amplitude. This is strong evidence of the modulation of the $f > f_{\mathrm{ce}}$ multiband electrostatic waves by the low-frequency oblique ion-scale waves.

The basic features of the $f > f_{\mathrm{ce}}$ multiband electrostatic waves are summarized as: (1) the frequency bands are located either between nf_{ce} and $(n + 1)f_{\mathrm{ce}}$ ($n = 1, 2, 3$, and 4) or near mf_{ce} ($m = 4, 5, 6$, and 7); (2) the frequency difference between two neighboring bands is about f_{ce}; and (3) the waves can be modulated by low-frequency electromagnetic waves.

4. Summary and Discussion

This Letter provides observational evidence of two new types of multiband electrostatic waves beyond the multiband electrostatic waves near f_{ce} found by Malaspina et al. (2020, 2021): one is most (or all) of the frequency bands below f_{ce}, and the other is all of the frequency bands above f_{ce}. Their observational features are explored in Section 3. Here, we proceed with further discussions on their mode nature and excitation mechanism.

The wave frequency and wavevector $\boldsymbol{k}$ in the plasma frame are the key parameters in determining the mode nature. Due to the Doppler frequency shift induced by the bulk flow of the solar wind particles, the relation between the wave frequency in the plasma frame f_{pl} and the frequency in the spacecraft frame f_{sc} is given as

$$2\pi f_{\mathrm{sc}} = 2\pi f_{\mathrm{pl}} + \boldsymbol{k} \cdot \boldsymbol{V}_0. \tag{1}$$

There are three possibilities associated with the wave frequency: (1) $f_{\mathrm{pl}} \ll f_{\mathrm{sc}}$; (2) $f_{\mathrm{pl}} \sim f_{\mathrm{sc}}$; and (3) $f_{\mathrm{pl}} \gg f_{\mathrm{sc}}$. The first possibility corresponds to $2\pi f_{\mathrm{sc}} \simeq \boldsymbol{k} \cdot \boldsymbol{V}_0$, which results in two predictions, i.e., the wavenumber along $\boldsymbol{V}_0$ approximates as $k_{V_0} \sim 2\pi f_{\mathrm{sc}}/V_0$, and the wave phase speed $v_p = 2\pi f_{\mathrm{pl}}/k$ is much smaller than V_0. In the second possibility, the wavenumber can be still approximated by the expression $k_{V_0} \sim 2\pi f_{\mathrm{sc}}/V_0$. The third possibility occurs as the wave propagates against $\boldsymbol{V}_0$, in
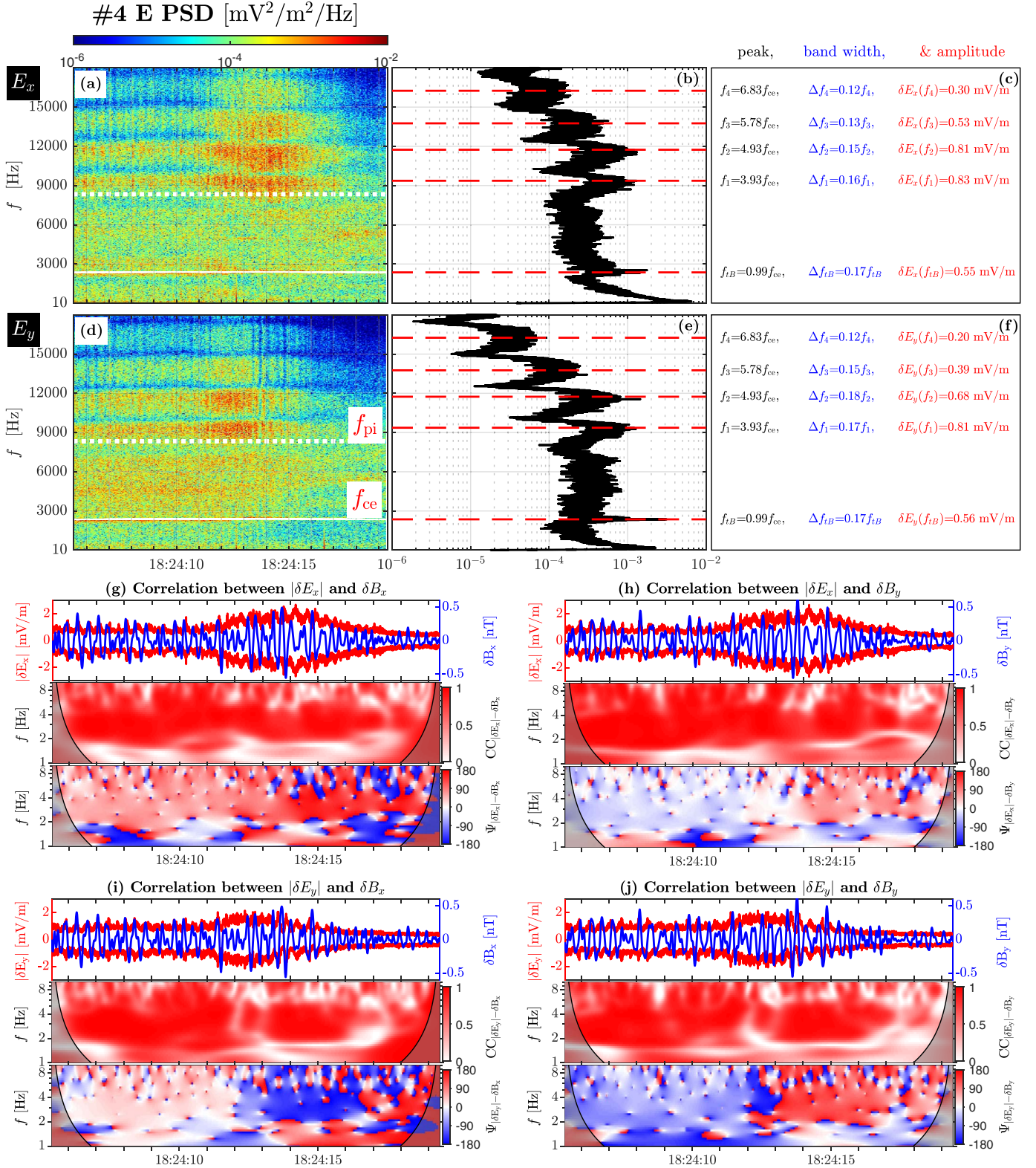
Figure 4. The PSDs of the electric field components E_x and E_y and the wave parameters in Event #4. Panels (a)−(g): the description is the same as those in Figure 2. The solid and dashed white curves represent the electron cyclotron frequency f_{ce} and the ion plasma frequency f_{pi}, respectively. Panels (h)−(k): the correlation analysis between the electric field strength $|\delta E_{x,y}|$ of the $f > f_{ce}$ multiband electrostatic waves and the magnetic field perturbation $\delta B_{x,y}$ of oblique ion-scale waves; from top to bottom panels, the waveform of $\pm|\delta E_{x,y}|$ and $\delta B_{x,y}$, the correlation coefficients $CC_{|\delta E_{x,y}|-\delta B_{x,y}}$, and the correlation phase differences $\Psi_{|\delta E_{x,y}|-\delta B_{x,y}}$.

which $f_{pl} \simeq -\mathbf{k} \cdot \mathbf{V}_0/2\pi$ and $k_{V_0} \gg 2\pi f_{sc}/V_0$, and this possibility is excluded because there is no plasma eigenmode that has the varying phase speed identical to the solar wind speed.

For the mode nature of the $f < f_{ce}$ multiband electrostatic waves, since there is no eigenmode of the plasma wave existing at multiple frequencies shown in Events #1 and #2, we can exclude
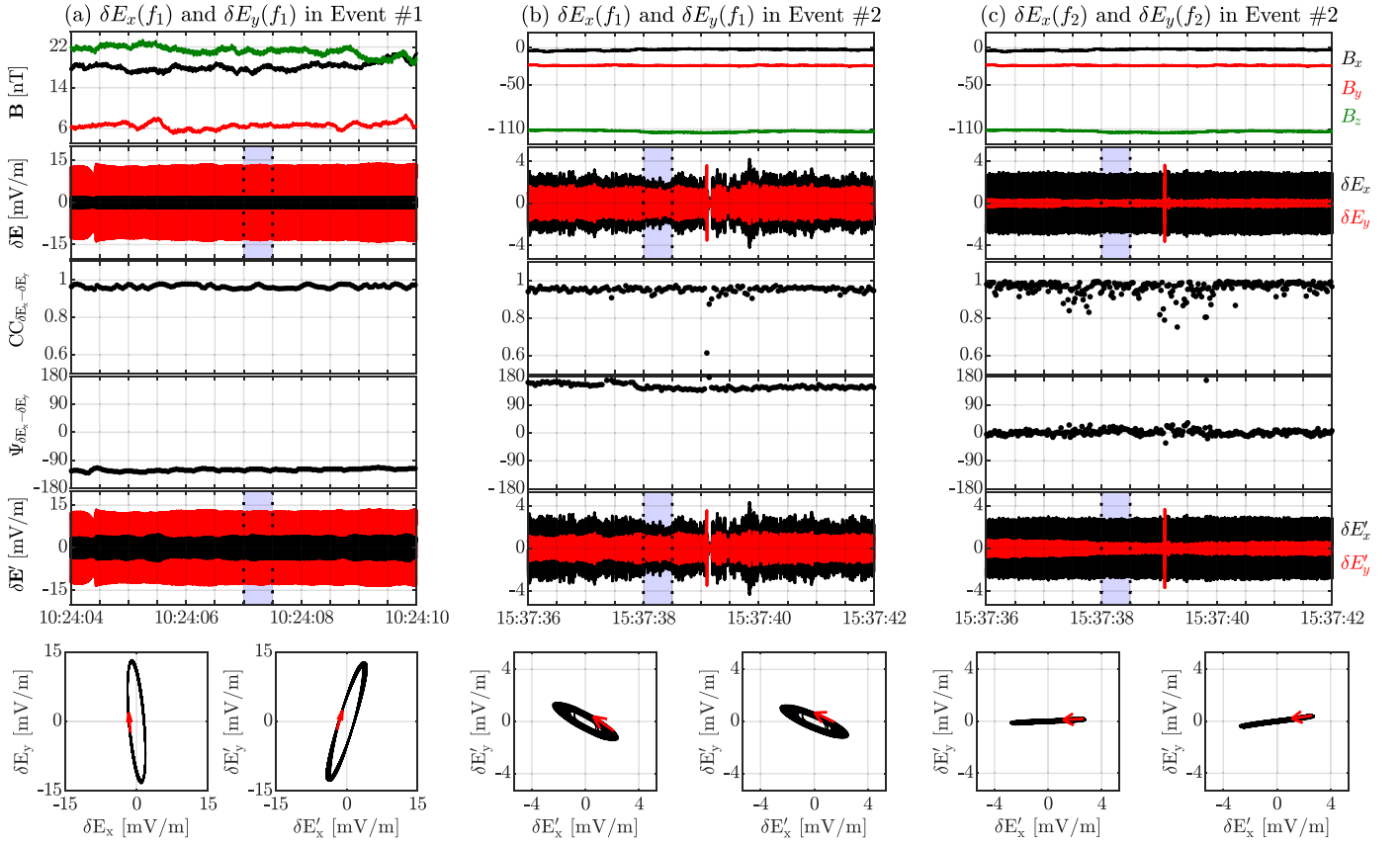
Figure 5. The δE_x and δE_y values of the three typical waves: (a) the first band wave in Event #1, (b) the first band wave in Event #2, and (c) the second band wave in Event #2. From top to bottom, the magnetic field components in spacecraft coordinates, the filtered δE_x and δE_y in spacecraft coordinates, the correlation coefficient $CC_{\delta E_x - \delta E_y}$ between δE_x and δE_y, the phase difference $\Psi_{\delta E_x - \delta E_y}$ between δE_x and δE_y, $\delta E_x'$ and $\delta E_y'$ in a frame in which $B_y' = 0$ (panel (a)) and in a frame in which $B_x' = 0$ (panels (b) and (c)), and hodograms for two electric field components during the time interval between two dotted lines. $CC_{\delta E_x - \delta E_y}$ and $\Psi_{\delta E_x - \delta E_y}$ are averaged over the time interval of $10/f_{peak}$, where f_{peak} corresponds to the frequency of the power peak in each frequency band.

the second possibility of the wave frequency in the plasma frame, i.e., $f_{pl} \sim f_{sc}$. According to f_{sc} and V_0 in Events #1 and #2, the wave scale is approximated as $\lambda = 2\pi/k_{V_0} = V_0/f_1 \sim 1.4$ km in Event #1 and $\lambda = 1.0$ km in Event #2 in the first frequency band. Due to the ion (electron) inertial length being $\lambda_p \simeq 6.0$ km ($\lambda_e \simeq 0.14$ km) in Event #1 and $\lambda_p \simeq 6.7$ km ($\lambda_e \simeq 0.16$ km) in Event #2, the first frequency band wave is located on a sub-ion scale. For higher frequency bands with f_n, the wave scale is about $\lambda(f_1/f_n)$, and the wave scale can even extend down to the electron scale, e.g., $\sim$0.08 km for the f_{12} band wave in Event #2. Therefore, the candidate for the observed (quasi-)electrostatic mode between the ion and electron scales could be the ion Bernstein wave, the ion acoustic (or beam) wave, or the lower-hybrid wave. For the ion Bernstein wave, the frequency difference between two neighboring bands is on the order of the proton cyclotron frequency, which is inconsistent with the frequency feature, i.e., $f_2 - f_1 \simeq 0.25 f_{ce}$ in Event #1 and $f_2 - f_1 \simeq 0.08 f_{ce}$ in Event #2. As a consequence, the mode nature of the $f < f_{ce}$ multiband electrostatic waves could be the ion acoustic (or beam) wave or the lower-hybrid wave.

In order to further identify the wave mode, we analyze the correlation between two electric field components for the first frequency band wave in Event #1 and the first and second band waves in Event #2, as shown in Figure 5. Mozer et al. (2020, 2021a, 2021b) have explored the ion acoustic waves that have at least the following observational features: (1) the phase difference $\Psi_{\delta E_x - \delta E_y}$ between δE_x and δE_y in the spacecraft frame of 0° or

180° (linear polarization); and (2) $|\delta E_y'| \ll |\delta E_x'|$ in a frame where $B_y' = 0$ through the rotation of the magnetic field data in the $x - y$ plane. From Figure 5, we find that the first frequency band waves in Event #1 exhibit left-handed elliptical polarization in the $x - y$ plane, i.e., $\Psi_{\delta E_x - \delta E_y} \sim -120°$ and $|\delta E_x'| \sim 3|\delta E_y'|$, which are not consistent with the two features of ion acoustic waves. Figure 5 also shows $\Psi_{\delta E_x - \delta E_y} \sim 150°$ and $|\delta E_x'| \sim 2|\delta E_y'|$ for the first frequency band wave in Event #2 and $\Psi_{\delta E_x - \delta E_y} \sim 3°$ and $|\delta E_x'| \sim 5|\delta E_y'|$ for the second frequency band wave. The former exhibits right-handed elliptical polarization, and the latter is linearly polarized in the $x–y$ plane. We note that due to $|B_x| \ll |B_y|$ in the spacecraft frame in Event #2, we rotate the magnetic field data in a frame in which $B_x' = 0$. Although the values of $\Psi_{\delta E_x - \delta E_y}$ of the first and second band waves in Event #2 are similar to feature (1) of ion acoustic waves, both the waves have a large electric component perpendicular to the local magnetic field, and this is different from feature (2). Consequently, we can exclude the possibility of an ion acoustic wave propagating along the magnetic field. However, we cannot exclude the possibility of an oblique ion acoustic wave.

We also analyze the electric field distribution of one $f < f_{ce}$ electrostatic wave event ($\sim$11:31:49−11:32:02 UTC) in which the magnetic field is nearly located in the spacecraft spin plane (e.g., $B_z / \sqrt{B_x^2 + B_y^2} \sim 0.3$), and we find the electric field component perpendicular to the magnetic field $E_\perp$ is much stronger than in the parallel electric field component $E_\parallel$.

Consequently, we can exclude the possibility of the parallel acoustic wave again. However, since highly oblique ion acoustic waves and lower-hybrid waves can have $E_\perp \gg E_\parallel$ (e.g., Zhao et al. 2014; Zhao 2015; Narita & Marsch 2015), we still cannot identify the nature of the observed waves.

No matter whether the wave mode is the oblique acoustic (or beam) wave or the lower-hybrid wave, the excitation mechanism of the $f < f_{ce}$ multiband electrostatic waves could be closely related to the relative drift between different particle components. Previous theoretical works have found that the ion acoustic (or beam) waves can be excited by the ion beams (e.g., Gary & Omidi 1987), and the lower-hybrid waves can be driven by the electron heat flux instability in the solar wind (e.g., Sun et al. 2021). These two kinds of free energy could exist in the heliospheric current sheet.

Regarding the mode nature of the $f > f_{ce}$ multiband electrostatic waves in Events #3 and #4, we propose they are electron Bernstein waves. This conclusion is based on the following facts. (1) The frequency difference between neighboring bands is about f_{ce}, which is consistent with the mode feature of electron Bernstein waves. (2) The observed frequency distributions are similar to that detected in planetary space environments (e.g., Kennel et al. 1970; Hospodarsky et al. 2008; Meredith et al. 2009; Li et al. 2020; Teng et al. 2021; Zhang et al. 2021). And, (3) linear instability theory and simulation have explored the appearance of electron Bernstein waves at frequencies in the range of nf_{ce} and $(n+1)f_{ce}$ (e.g., Wu et al. 2020).

Moreover, since the wave frequency distribution in Event #3 is similar to the predictions of linear instability theory and simulation, we propose that these waves are locally excited. According to the resonant condition between electrons and electron Bernstein waves, $2\pi f = k_\parallel v_{res} + 2\pi n f_{ce}$, we can estimate the resonant energy $E_{res} = m_e v_{res}^2 / 2$ for the electrons contributing to the local excitation of the observed waves, where $k_\parallel$ is the parallel wavenumber and n is the integer. E_{res} is about $30-3000$ eV when we consider $v_{res} \sim 2\pi f_{ce}/k_\parallel$, $f_{ce} \sim 3300$ Hz, $k_\parallel = (1 - 10)/\lambda_e$, and $\lambda_e = 0.16$ km. From the pitch angle distribution of electrons with an energy of $30-3000$ eV (not shown), we find the existence of two electron beam components parallel and antiparallel to the magnetic field and one electron component with the perpendicular temperature larger than the parallel temperature in which the electron energy spans $\sim 40-150$ eV. These electron components may be responsible for the local excitation of the observed waves in Event #3.

For the waves in Event #4, considering that the linear instability timescale $\sim 1/f_{ce}$ is much smaller than the timescale of the modulation by oblique ion-scale waves, $\sim 1/f_{cp}$, we propose that the wave source is more likely nonlocal. However, we cannot totally exclude the possibility of local excitation, such that the $f > f_{ce}$ multiband electrostatic waves are excited by the unstable electron distribution function modulated by oblique ion-scale waves. A detailed instability analysis under the local plasma parameters will be given in the future.

Lastly, we note that in addition to multiband electrostatic waves observed in and near the heliospheric current sheet, there exist Type B narrowband electrostatic waves, low-frequency ion-scale waves, and whistler waves (see Figure 1). These plentiful wave activities are closely related to both ion and electron dynamics. Therefore, our results provide valuable clues to further explore the coupling process between various waves and particle dynamics in the near-Sun solar wind.

ORCID iDs

Chen Shi ⓘ https://orcid.org/0000-0002-9166-1036
Jinsong Zhao ⓘ https://orcid.org/0000-0002-3859-6394
David M. Malaspina ⓘ https://orcid.org/0000-0003-1191-1558
Stuart D. Bale ⓘ https://orcid.org/0000-0002-1989-3596
Xiangcheng Dong ⓘ https://orcid.org/0000-0001-6519-8706
Dejin Wu ⓘ https://orcid.org/0000-0003-2418-5508

References

Ashour-Abdalla, M., & Kennel, C. F. 1978, JGR, 83, 1531
Bale, S. D., Goetz, K., Harvey, P. R., et al. 2016, SSRv, 204, 49
Bastian, T. S., Benz, A. O., & Gary, D. E. 1998, ARA&A, 36, 131
Chen, L., Wu, D. J., Xiang, L., et al. 2020, ApJ, 904, 193
Fox, N. J., Velli, M. C., Bale, S. D., et al. 2016, SSRv, 204, 7
Gary, S. P., & Omidi, N. 1987, JPlPh, 37, 45
Hospodarsky, G. B., Averkamp, T. F., Kurth, W. S., et al. 2008, JGRA, 113, A12206
Kasper, J. C., Abiad, R., Austin, G., et al. 2016, SSRv, 204, 131
Kennel, C. F., Scarf, F. L., Fredricks, R. W., et al. 1970, JGR, 75, 6136
Li, W. Y., Graham, D. B., Khotyaintsev, Y. V., et al. 2020, NatCo, 11, 141
Ma, J., Gao, X., Yang, Z., et al. 2021, ApJ, 918, 26
Malaspina, D. M., Ergun, R. E., Bolton, M., et al. 2016, JGRA, 121, 5088
Malaspina, D. M., Halekas, J., Berčič, L., et al. 2020, ApJS, 246, 21
Malaspina, D. M., Wilson, L. B., Ergun, R. E., et al. 2021, A&A, 650, A97
Meredith, N. P., Horne, R. B., Thorne, R. M., et al. 2009, JGRA, 114, A07218
Moncuquet, M., Meyer-Vernet, N., Issautier, K., et al. 2020, ApJS, 246, 44
Mozer, F. S., Bonnell, J. W., Bowen, T. A., et al. 2020, ApJ, 901, 107
Mozer, F. S., Bonnell, J. W., Halekas, J. S., et al. 2021a, ApJ, 908, 26
Mozer, F. S., Vasko, I. Y., & Verniero, J. L. 2021b, ApJL, 919, L2
Narita, Y., & Marsch, E. 2015, ApJ, 805, 24
Shi, C., Zhao, J., Sun, H., et al. 2020, ApJ, 902, 151
Sun, H., Zhao, J., Liu, W., et al. 2021, ApJL, 916, L4
Teng, S., Wu, Y., Guo, R., et al. 2021, GeoRL, 48, e94559
Umeda, T., Ashour-Abdalla, M., Schriver, D., et al. 2007, JGRA, 112, A04212
Wu, Y., Tao, X., Liu, X., et al. 2020, GeoRL, 47, e87649
Zhang, X., Angelopoulos, V., Artemyev, A. V., et al. 2021, JGRA, 126, e28743
Zhao, J. 2015, PhPl, 22, 042115
Zhao, J. S., Voitenko, Y., Yu, M. Y., et al. 2014, ApJ, 793, 107
Zhou, X., Muñoz, P. A., Büchner, J., et al. 2020, ApJ, 891, 92